

## **COPYRIGHT NOTICE**

© 2018 Optical Society of America.

Users may use, reuse, and build upon the article, or use the article for text or data mining, so long as such uses are for non-commercial purposes and appropriate attribution is maintained.

All other rights are reserved.



# Instrumental, optical and geometrical parameters affecting time-gated diffuse optical measurements: a systematic study

ANURAG BEHERA,<sup>1</sup> LAURA DI SIENO,<sup>1,\*</sup> ANTONIO PIFFERI,<sup>1,2</sup> FABRIZIO MARTELLI,<sup>3</sup> AND ALBERTO DALLA MORA<sup>1</sup>

<sup>1</sup>Politecnico di Milano, Dipartimento di Fisica, Piazza Leonardo da Vinci 32, 20133 Milano, Italy

<sup>2</sup>Consiglio Nazionale delle Ricerche, Istituto di Fotonica e Nanotecnologie, Piazza Leonardo da Vinci 32, 20133 Milano, Italy

<sup>3</sup>Università degli Studi di Firenze, Dipartimento di Fisica e Astronomia, Via G. Sansone 1, 50019 Sesto Fiorentino, Firenze, Italy

\*[laura.disieno@polimi.it](mailto:laura.disieno@polimi.it)

**Abstract:** In time-domain diffuse optics the sensitivity to localized absorption changes buried inside a diffusive medium depends strongly on the interplay between instrumental, optical and geometrical parameters, which can hinder the theoretical advantages of novel measurement strategies like the short source-detector distance approach. Here, we present a study based on experimental measurements and simulations to comprehensively evaluate the effect of all different parameters. Results are evaluated exploiting standardized figures of merit, like contrast and contrast-to-noise ratio, to quantify the system sensitivity to deep localized absorption perturbations. Key findings show that the most critical hardware parameter is the memory effect which ultimately limits the dynamic range. Further, a choice of the source-detector distance around 10 mm seems to be a good compromise to compensate non-idealities in practical systems still preserving the advantages of short distances. This work provides both indications for users about the best measurement conditions and strategies, and for technology developers to identify the most crucial hardware features in view of next generation diffuse optics systems.

© 2018 Optical Society of America under the terms of the [OSA Open Access Publishing Agreement](#)

## References and links

1. A. Yodh and B. Chance, "Spectroscopy and imaging with diffusing light," *Phys. Today* **48**(3), 34–41 (1995).
2. T. Durduran, R. Choe, W. B. Baker, and A. G. Yodh, "Diffuse optics for tissue monitoring and tomography," *Rep. Prog. Phys.* **73**(7), 076701 (2010).
3. I. Bargigia, A. Nevin, A. Farina, A. Pifferi, C. D'Andrea, M. Karlsson, P. Lundin, G. Somesfalean, and S. Svanberg, "Diffuse optical techniques applied to wood characterisation," *J. Near Infrared Spectrosc.* **21**(4), 259–268 (2013).
4. A. Bellincontro, A. Taticchi, M. Servili, S. Esposto, D. Farinelli, and F. Mencarelli, "Feasible application of a portable nir-AOTF tool for on-field prediction of phenolic compounds during the ripening of olives for oil production," *J. Agric. Food Chem.* **60**(10), 2665–2673 (2012).
5. P. Taroni, G. Quarto, A. Pifferi, F. Ieva, A. M. Paganoni, F. Abbate, N. Balestreri, S. Menna, E. Cassano, and R. Cubeddu, "Optical identification of subjects at high risk for developing breast cancer," *J. Biomed. Opt.* **18**(6), 060507 (2013).
6. L. Di Sieno, G. Bettega, M. Berger, C. Hamou, M. Aribert, A. D. Mora, A. Puszka, H. Grateau, D. Contini, L. Hervé, J.-L. Coll, J.-M. Dinten, A. Pifferi, and A. Planat-Chrétien, "Toward noninvasive assessment of flap viability with time-resolved diffuse optical tomography: a preclinical test on rats," *J. Biomed. Opt.* **21**(2), 025004 (2016).
7. A. Pifferi, A. Torricelli, P. Taroni, A. Bassi, E. Chikoidze, E. Giambattistelli, and R. Cubeddu, "Optical biopsy of bone tissue: a step toward the diagnosis of bone pathologies," *J. Biomed. Opt.* **9**(3), 474–480 (2004).
8. L. Enfield, G. Cantanhede, M. Douek, V. Ramalingam, A. Purushotham, J. Hebden, and A. Gibson, "Monitoring the response to neoadjuvant hormone therapy for locally advanced breast cancer using three-dimensional time-resolved optical mammography," *J. Biomed. Opt.* **18**(5), 056012 (2013).
9. A. Torricelli, V. Quaresima, A. Pifferi, G. Biscotti, L. Spinelli, P. Taroni, M. Ferrari, and R. Cubeddu, "Mapping of calf muscle oxygenation and haemoglobin content during dynamic plantar flexion exercise by multi-channel time-resolved near-infrared spectroscopy," *Phys. Med. Biol.* **49**(5), 685–699 (2004).
10. D. Contini, L. Zucchelli, L. Spinelli, M. Caffini, R. Re, A. Pifferi, R. Cubeddu, and A. Torricelli, "Review: Brain

- and muscle near infrared spectroscopy/imaging techniques,” *J. Near Infrared Spectrosc.* **20**(1), 15–27 (2012).
11. G. Quarto, L. Spinelli, A. Pifferi, A. Torricelli, R. Cubeddu, F. Abbate, N. Balestreri, S. Menna, E. Cassano, and P. Taroni, “Estimate of tissue composition in malignant and benign breast lesions by time-domain optical mammography,” *Biomed. Opt. Express* **5**(10), 3684–3698 (2014).
  12. A. Torricelli, D. Contini, A. Pifferi, M. Caffini, R. Re, L. Zucchelli, and L. Spinelli, “Time domain functional NIRS imaging for human brain mapping,” *Neuroimage* **85**(Pt 1), 28–50 (2014).
  13. M. Ferrari and V. Quaresima, “A brief review on the history of human functional near-infrared spectroscopy (fNIRS) development and fields of application,” *Neuroimage* **63**(2), 921–935 (2012).
  14. S. L. Jacques, “Time resolved propagation of ultrashort laser pulses within turbid tissues,” *Appl. Opt.* **28**(12), 2223–2229 (1989).
  15. F. Martelli, T. Binzoni, A. Pifferi, L. Spinelli, A. Farina, and A. Torricelli, “There’s plenty of light at the bottom: statistics of photon penetration depth in random media,” *Sci. Rep.* **6**(1), 27057 (2016).
  16. D. T. Delpy and M. Cope, “Quantification in tissue near-infrared spectroscopy,” *Appl. Opt.* **35**(2), 649 (1997).
  17. T. Durduran, R. Choe, J. P. Culver, L. Zubkov, M. J. Holbake, J. Giammarco, B. Chance, and A. G. Yodh, “Bulk optical properties of healthy female breast tissue,” *Phys. Med. Biol.* **47**(16), 2847–2861 (2002).
  18. A. D. Mora, D. Contini, S. Arridge, F. Martelli, A. Tosi, G. Boso, A. Farina, T. Durduran, E. Martinenghi, A. Torricelli, and A. Pifferi, “Towards next-generation time-domain diffuse optics for extreme depth penetration and sensitivity,” *Biomed. Opt. Express* **6**(5), 1749–1760 (2015).
  19. L. Di Sieno, J. Nissinen, L. Hallman, E. Martinenghi, D. Contini, A. Pifferi, J. Kostamovaara, and A. D. Mora, “Miniaturized pulsed laser source for time-domain diffuse optics routes to wearable devices,” *J. Biomed. Opt.* **22**(8), 1–9 (2017).
  20. L. D. Sieno, A. D. Mora, G. Boso, A. Tosi, A. Pifferi, R. Cubeddu, and D. Contini, “Diffuse optics using a dual window fast-gated counter,” *Appl. Opt.* **53**(31), 7394–7401 (2014).
  21. A. Pifferi, D. Contini, A. D. Mora, A. Farina, L. Spinelli, and A. Torricelli, “New frontiers in time-domain diffuse optics, a review,” *J. Biomed. Opt.* **21**(9), 091310 (2016).
  22. M. Renna, M. Buttafava, A. Behera, M. Zanoletti, L. Di Sieno, A. Dalla Mora, D. Contini, and A. Tosi, “Eight-wavelength, dual detection-channel instrument for near-infrared time-resolved diffuse optical spectroscopy,” *IEEE J. Sel. Top. Quantum Electron.* **25**(1), 1 (2019).
  23. F. Scholkmann, S. Kleiser, A. J. Metz, R. Zimmermann, J. Mata Pavia, U. Wolf, and M. Wolf, “A review on continuous wave functional near-infrared spectroscopy and imaging instrumentation and methodology,” *Neuroimage* **85**(Pt 1), 6–27 (2014).
  24. A. Torricelli, A. Pifferi, L. Spinelli, R. Cubeddu, F. Martelli, S. Del Bianco, and G. Zaccanti, “Time-Resolved Reflectance at Null Source-Detector Separation: Improving Contrast and Resolution in Diffuse Optical Imaging,” *Phys. Rev. Lett.* **95**(7), 078101 (2005).
  25. A. Pifferi, A. Torricelli, L. Spinelli, D. Contini, R. Cubeddu, F. Martelli, G. Zaccanti, A. Tosi, A. Dalla Mora, F. Zappa, and S. Cova, “Time-Resolved Diffuse Reflectance Using Small Source-Detector Separation and Fast Single-Photon Gating,” *Phys. Rev. Lett.* **100**(13), 138101 (2008).
  26. A. Dalla Mora, A. Tosi, F. Zappa, S. Cova, D. Contini, A. Pifferi, L. Spinelli, A. Torricelli, and R. Cubeddu, “Fast-gated single-photon avalanche diode for wide dynamic range near infrared spectroscopy,” *Sel. Top. Quantum Electron.* **16**(4), 1023–1030 (2010).
  27. A. Tosi, A. Dalla Mora, F. Zappa, A. Gulinatti, D. Contini, A. Pifferi, L. Spinelli, A. Torricelli, and R. Cubeddu, “Fast-gated single-photon counting technique widens dynamic range and speeds up acquisition time in time-resolved measurements,” *Opt. Express* **19**(11), 10735–10746 (2011).
  28. L. Di Sieno, H. Wabnitz, A. Pifferi, M. Mazurenka, Y. Hoshi, A. Dalla Mora, D. Contini, G. Boso, W. Becker, F. Martelli, A. Tosi, and R. Macdonald, “Characterization of a time-resolved non-contact scanning diffuse optical imaging system exploiting fast-gated single-photon avalanche diode detection,” *Rev. Sci. Instrum.* **87**(3), 035118 (2016).
  29. A. Puszka, L. Di Sieno, A. D. Mora, A. Pifferi, D. Contini, A. Planat-Chrétien, A. Koenig, G. Boso, A. Tosi, L. Hervé, and J.-M. Dinten, “Spatial resolution in depth for time-resolved diffuse optical tomography using short source-detector separations,” *Biomed. Opt. Express* **6**(1), 1–10 (2015).
  30. E. Alerstam, T. Svensson, S. Andersson-Engels, L. Spinelli, D. Contini, A. Dalla Mora, A. Tosi, F. Zappa, and A. Pifferi, “Single-fiber diffuse optical time-of-flight spectroscopy,” *Opt. Lett.* **37**(14), 2877–2879 (2012).
  31. H. Wabnitz, D. R. Taubert, M. Mazurenka, O. Steinkellner, A. Jelzow, R. Macdonald, D. Milej, P. Sawosz, M. Kacprzak, A. Liebert, R. Cooper, J. Hebden, A. Pifferi, A. Farina, I. Bargigia, D. Contini, M. Caffini, L. Zucchelli, L. Spinelli, R. Cubeddu, and A. Torricelli, “Performance assessment of time-domain optical brain imagers, part I: basic instrumental performance protocol,” *J. Biomed. Opt.* **19**(8), 086010 (2014).
  32. D. Contini, A. Dalla Mora, L. Spinelli, A. Farina, A. Torricelli, R. Cubeddu, F. Martelli, G. Zaccanti, A. Tosi, G. Boso, F. Zappa, and A. Pifferi, “Effects of time-gated detection in diffuse optical imaging at short source-detector separation,” *J. Phys. D Appl. Phys.* **48**(4), 045401 (2015).
  33. A. Dalla Mora, D. Contini, A. Pifferi, R. Cubeddu, A. Tosi, and F. Zappa, “Afterpulse-like noise limits dynamic range in time-gated applications of thin-junction silicon single-photon avalanche diode,” *Appl. Phys. Lett.* **100**(24), 241111 (2012).
  34. A. Dalla Mora, A. Tosi, D. Contini, L. Di Sieno, G. Boso, F. Villa, and A. Pifferi, “Memory effect in silicon time-gated single-photon avalanche diodes,” *J. Appl. Phys.* **117**(11), 114501 (2015).

35. H. Wabnitz, A. Jelzow, M. Mazurenka, O. Steinkellner, R. Macdonald, D. Milej, N. Żołek, M. Kacprzak, P. Sawosz, R. Maniewski, A. Liebert, S. Magazov, J. Hebden, F. Martelli, P. Di Ninni, G. Zaccanti, A. Torricelli, D. Contini, R. Re, L. Zucchelli, L. Spinelli, R. Cubeddu, and A. Pifferi, “Performance assessment of time-domain optical brain imagers, part 2: nEUROpt protocol,” *J. Biomed. Opt.* **19**(8), 086012 (2014).
36. G. Boso, A. Dalla Mora, A. Della Frera, and A. Tosi, “Fast-gating of single-photon avalanche diodes with 200 ps transitions and 30 ps timing jitter,” *Sens. Actuators A Phys.* **191**, 61–67 (2013).
37. A. Tosi, A. Dalla Mora, A. Della Frera, F. Acerbi, A. Bahgat Shehata, and F. Zappa, “Advanced single photon counting instrumentation for SPADs,” *Proc. SPIE* **7945**, 79452O (2011).
38. L. Spinelli, M. Botwicz, N. Zolek, M. Kacprzak, D. Milej, P. Sawosz, A. Liebert, U. Weigel, T. Durduran, F. Foschum, A. Kienle, F. Baribeau, S. Leclair, J.-P. Bouchard, I. Noiseux, P. Gallant, O. Mermut, A. Farina, A. Pifferi, A. Torricelli, R. Cubeddu, H.-C. Ho, M. Mazurenka, H. Wabnitz, K. Klauenberg, O. Bodnar, C. Elster, M. Bénazech-Lavoué, Y. Bérubé-Lauzière, F. Lesage, D. Khoptyar, A. A. Subash, S. Andersson-Engels, P. Di Ninni, F. Martelli, and G. Zaccanti, “Determination of reference values for optical properties of liquid phantoms based on Intralipid and India ink,” *Biomed. Opt. Express* **5**(7), 2037–2053 (2014).
39. F. Martelli, A. Pifferi, D. Contini, L. Spinelli, A. Torricelli, H. Wabnitz, R. Macdonald, A. Sassaroli, and G. Zaccanti, “Phantoms for diffuse optical imaging based on totally absorbing objects, part 1: Basic concepts,” *J. Biomed. Opt.* **18**(6), 066014 (2013).
40. F. Martelli, P. Di Ninni, G. Zaccanti, D. Contini, L. Spinelli, A. Torricelli, R. Cubeddu, H. Wabnitz, M. Mazurenka, R. Macdonald, A. Sassaroli, and A. Pifferi, “Phantoms for diffuse optical imaging based on totally absorbing objects, part 2: experimental implementation,” *J. Biomed. Opt.* **19**(7), 076011 (2014).
41. A. Sassaroli, A. Pifferi, D. Contini, A. Torricelli, L. Spinelli, H. Wabnitz, P. Di Ninni, G. Zaccanti, and F. Martelli, “Forward solvers for photon migration in the presence of highly and totally absorbing objects embedded inside diffusive media,” *J. Opt. Soc. Am. A* **31**(3), 460–469 (2014).
42. D. V. O’ Connor and D. Phillips, *Time-Correlated Single Photon Counting* (Academic Press, 1984).
43. Figshare, “Dependence of contrast and CNR on the IRF full-width at half-maximum (FWHM),” <https://doi.org/10.6084/m9.figshare.6731279>.
44. Figshare, “Dependence of contrast and CNR on the fast tail amplitude (A1),” <https://doi.org/10.6084/m9.figshare.6736532>.
45. Figshare, “Dependence of contrast and CNR on the fast tail slope (Tau1),” <https://doi.org/10.6084/m9.figshare.6736547>.
46. Figshare, “Dependence of contrast and CNR on the memory tail amplitude (A2),” <https://doi.org/10.6084/m9.figshare.6736550>.
47. Figshare, “Dependence of contrast and CNR on the average laser power (P),” <https://doi.org/10.6084/m9.figshare.6736553>.
48. Figshare, “Dependence of contrast and CNR on the optical responsivity (R),” <https://doi.org/10.6084/m9.figshare.6736556>.
49. Figshare, “Dependence of contrast and CNR on the dark count rate (DCR),” <https://doi.org/10.6084/m9.figshare.6736559>.
50. Figshare, “Dependence of contrast and CNR on the afterpulsing (AP),” <https://doi.org/10.6084/m9.figshare.6736568>.
51. Figshare, “Dependence of contrast and CNR on the acquisition time (Aqt),” <https://doi.org/10.6084/m9.figshare.6736574>.
52. Figshare, “Dependence of contrast and CNR on optical properties of background diffusive medium,” <https://doi.org/10.6084/m9.figshare.6736547>.

## 1. Introduction

Since decades light has been considered a powerful tool to analyze diffusive media [1] such as biological tissues [2], wood [3], fruits [4], etc. Indeed, both medium composition and microstructure are strictly connected to its optical properties (absorption –  $\mu_a$  – and reduced scattering –  $\mu_s'$  – coefficient, respectively). Therefore, light in the so-called “therapeutic window” (from 600 to 1100 nm, where tissues behave as low absorbing and highly scattering media) can be exploited to non-invasively gather information about relative concentration of tissue constituents for several diagnostic purposes [5–8], to monitor blood oxygenation in muscles [9,10], or to detect tumors [11] or localized functional activations in the brain [12,13], just to give a few examples.

Within this framework, time-domain (TD) diffuse optics relies on the injection of fast (~100 ps) light pulses into the medium and on the collection of the distribution of time of flight (DTOF) of the re-emitted photons at a certain distance (i.e. source-detector separation –  $\rho$  –) [14]. Since  $\mu_a$  and  $\mu_s'$  affect the DTOF in different ways, they can be recovered independently, provided that a proper model of photon migration is given. Another important

feature of the TD technique, for measurements performed in reflectance geometry, is the possibility to exploit the information about arrival time of photons to probe different depths into the investigated medium [15]. For its high information content, TD technique is considered attractive even if it requires more complex and expensive instrumentation with respect to systems operating in the continuous wave (CW) regime [16] or in the frequency-domain (FD) [17]. In particular, it has been recently demonstrated that CW instruments, at the level of ultimate performances, can reach a significantly lower penetration depth ( $\sim 3$  cm instead of  $\sim 6$  cm of TD technique for the same paradigmatic case) and have a sensitivity to localized heterogeneities (e.g. localized brain functional activation) orders of magnitude lower [18]. Further, during the last decade, many technological advancements for sources, detectors and time-tagging electronics had been achieved [19–21], thus allowing new TD systems [22] to reach a level of complexity, dimension and cost closer to CW devices [23].

To go in the direction of wearable devices and to simultaneously achieve the ultimate performances from TD technique, two requirements are needed [18]: availability of dense grids of fast time-gated ( $\sim 100$  ps) detectors to maximize the photon collection area ( $\sim 1$  cm<sup>2</sup>) and similar dense grids of laser injection points to maximize the amount of light that can be injected into the tissue without exceeding the safety limits for skin. For this purpose, source and detectors have to be placed close to each other (i.e. in the so called small  $\rho$  approach) to maximize the tissue coverage. In principle, the small  $\rho$  brings advantages that have been studied in previous papers [24,25] that are: i) improved contrast at all photon arrival times along the DTOF; ii) improved spatial resolution due to higher photons confinement; iii) increased signal at all times. However, at small  $\rho$  ( $< 1$  cm), the number of early photons overcomes the number of late photons by orders of magnitude, thus saturating the detection chain with photons that only had the time to probe the tissue surface [24]. To avoid this, a detector with a wide dynamic range of 5-8 orders of magnitude is required, thus being able to detect the few late photons arriving after the burst of early ones. It was demonstrated that this is feasible by using a time-gated Single-Photon Avalanche Diode (SPAD) [26] in combination with suitable measurement strategies [27]. This allowed the use of the technique in several applications ranging from non-contact or single fiber spectroscopy to tomography and its application for medical imaging [6,28–30]. However, with respect to the estimated theoretical advantages using ideal systems [24], real measurements performed at small  $\rho$  showed non-idealities and limitations. In particular, these are due to: i) system characteristics, ii) geometrical and optical conditions; iii) measurements strategy.

Most of the relevant system parameters are related to the shape of the Instrument Response Function – IRF – (i.e. the temporal response of the system taken as a whole) [31]. In particular, the key features are: i) Full-Width at Half-Maximum (FWHM); ii) fast (tens of ps) or slow (ns) decay tails [32]; iii) a specific source of noise termed *memory effect* [33,34], which sets a limit to the maximum achievable dynamic range. In addition, other system characteristics (such as the detector noise, the available laser power and the overall collection efficiency) can surely affect the sensitivity to small optical objects.

The geometrical conditions that can affect the measurement performance are the position and size of the optical perturbation to be detected, while the optical conditions are the background optical properties and the amount of perturbation with respect to the background. Of course, these are external factors related to the specific problem under study and out of the control of the operator. Among the controllable parameters, the source-detector distance  $\rho$  is crucial since it can severely affect the measurement outcome [24,32]. Other relevant issues to be considered are the temporal position of the enabling gating windows applied to the detector and the integration time of the acquisition.

In this work, a systematic experimental and theoretical study on the optimal conditions for short-distance measurements is carried out with a double aim: i) to provide a guide to scientists to choose the best conditions for measurements protocols and ii) to understand

which are the critical system parameters so as to provide to technology developers a set of relevant hardware features which can be considered key factors to maximize the performance of future generation of diffuse optics instruments. For what concerns the first aim, it is clearly of the utmost importance to get the best measurement results from existing systems. Just to give an idea, in many biomedical applications of diffuse optics (e.g. optical mammography, functional brain imaging, etc.) it is well known that the placement of optical fibers and the choice of the source-detector distance plays a fundamental role. Indeed, as discussed above, the use of a small  $\rho$  coupled to fast-gated acquisition is expected to improve the spatial resolution in measuring heterogeneous media. This can be relevant in applications like brain imaging or tumor characterization, where the spatial selectivity is important to reduce the contamination of the information from surrounding tissues. However, possible problems arising at short  $\rho$  (e.g. memory effect) can strongly affect the measurement, thus resulting into a dramatic loss of performance. Therefore, many times, there is the need to find a trade-off, which is done on the basis of the scientist's experience. Another crucial point when measuring heterogeneous biological tissues is the fine tuning of the system. For example, pulsed laser diodes often allow the user to optimize the power tune, forcing the choice between a condition with a more ideal shape of the IRF with low emitted power and a condition with broad laser pulses with high emitted power. Also in this case, a trade-off based on the experience of the operator is usually applied, often without a solid theoretical study.

The study presented here is restricted to absorption perturbations (thus with a reduced scattering coefficient in the inhomogeneity equal to the background). However, this case is paradigmatic for several medical applications such as functional near-infrared spectroscopy or tumor detection, where mainly variations in absorption are expected.

In this study, the effect of some of the above listed relevant parameters have been systematically studied both with phantom measurements (where a particular instrument has been tested in comparison to simulations) and with simulations (thus enabling to extend the previous results to other possible instruments, e.g. featuring a different IRF shape). Conclusions are drawn considering the standardized figure of merits (Contrast and Contrast-to-Noise Ratio) defined in the "nEUROPT" protocol [35], which is an internationally agreed procedure for the performance assessment of TD instruments. In this way, scientists can be supported in the choice of the best experimental conditions and measurement strategies to exploit at the best their system depending on the problem under study (e.g. detection of localized brain activation, tumor tissue characterization, etc.).

The paper is organized as follows: in Sec. 2 we describe the experimental setup, the simulation tool and the data analysis; Sec. 3 deals with the results obtained with phantom measurements and simulations; finally, in Sec. 4 we draw the conclusions of the work and discuss future perspectives.

## 2. Materials and methods

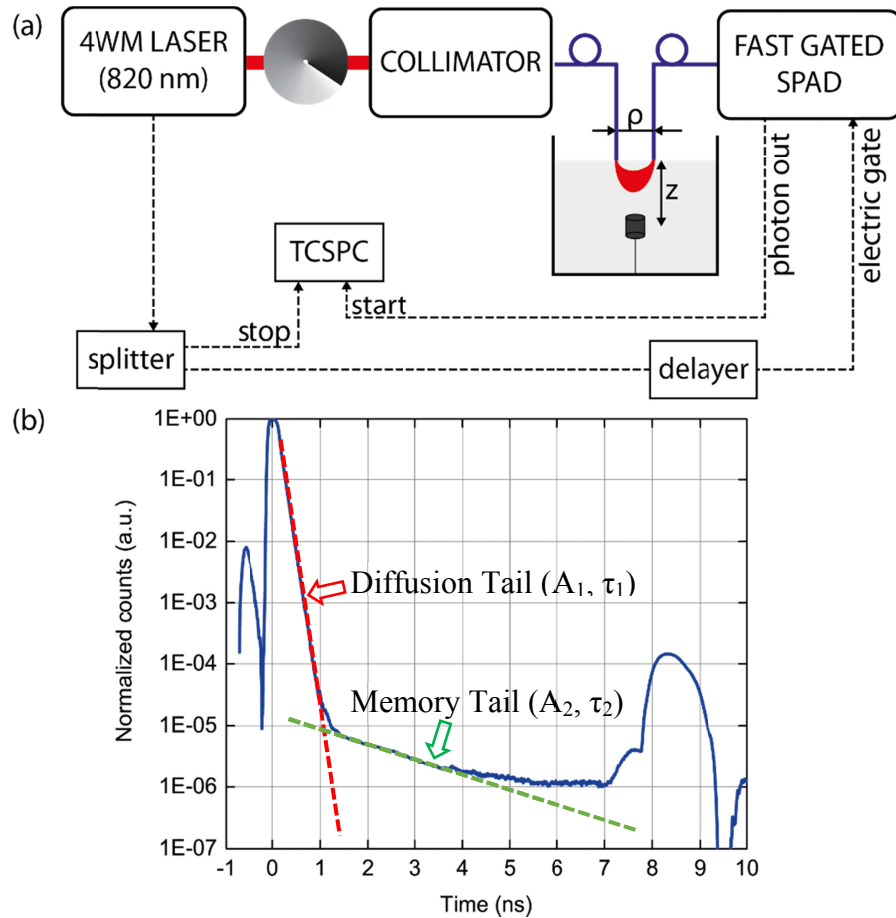


Fig. 1. (a) Schematics of the experimental setup used for measurements (dashed line: electrical connections; solid lines: optical path) and (b) reconstructed IRF of the setup.

### 2.1. Experimental setup

Figure 1(a) shows the schematics of the experimental setup. The light pulses (duration  $< 100$  ps FWHM, 40 MHz repetition rate, 90 mW average power) were provided by a laser prototype (Fianium Ltd, UK) based on four-wave mixing process at 820 nm wavelength. The light exiting the laser was then attenuated by means of a stack of variable optical attenuators, coupled into 50  $\mu\text{m}$  core diameter fiber through a collimator and sent into a liquid phantom (described in Sect. 2.2.1). Due to losses in the optical path between laser and sample, a maximum average power of about 50 mW was delivered to the phantom. Photons exiting from the medium were collected by a 200  $\mu\text{m}$  core diameter fiber at a variable  $\rho$  and then they were focused onto the detector (fast-gated SPAD, with an active area of 100  $\mu\text{m}$  diameter) [36]. When a photon impinges onto the detector, an avalanche is triggered and when it is sensed from the electronics inside the module, an output voltage pulse signal is generated (“photon out” in Fig. 1). Such a signal was fed to the “start” input of the Time-Correlated Single-Photon Counting (TCSPC) board (SPC 130, Becker and Hickl GmbH, Germany). The synchronism signal given by the laser (synchronous to the light pulse) was split into two. One half was sent to the “stop” input of the TCSPC board. Since the SPAD is normally OFF, the other half was used as triggering signal to enable the fast-gated SPAD within a well-defined time window (hereinafter “hardware gate”). In this way, the detector is switched ON in about

200 ps in order to allow the detection of photons within a 5 ns hardware gate. The different delays of the opening of the hardware gate were achieved by delaying the triggering signal through a home-made transmission-line based delay (minimum step: 25 ps) [37]. Following the procedure defined in the nEUROPt protocol, the optical perturbation (details in section 2.2.1) was immersed in the liquid medium in upright position thanks to a white-painted thin rigid wire, which was inserted from underneath. Figure 1(b) shows the reconstruction of the IRF of the setup acquired using the time-gated acquisition strategy as demonstrated in [27]. The IRF has two distinct exponentially decaying tails. First, the well known diffusion tail, with typical time constants ( $\tau_1$ ) of 80 ps. The second tail is the so called “Memory tail”, a slowly decaying tail that has been well described in [34]. It is due to an increase in the background noise during the hardware gate, which is proportional to number of photons impinging on the detector before its opening. For this reason, the contribution of the memory effect is higher when a short source-detector distance is used, due to the increase of early photons that are rejected – i.e. not detected – by the time-gating technique.

The memory effect is a signal dependent phenomenon, since its contribution to the background noise increases with increase in the number of photons impinging on the detector. It has a typical time constant ( $\tau_2$ ) of around 1800 ps. The memory amplitude ( $A_2$ ) is strongly dependent on the number of impinging photons.

## 2.2. Measurements

### 2.2.1. Phantom and optical perturbation (equivalent black volume)

The liquid phantom hosting the optical perturbation was dilution in water of Intralipid 20% and Higgins India ink [38]. The desired optical properties of the phantom were targeted by a precise proportion of Intralipid and India ink and by using their calibrated values for the scattering and absorption properties, respectively.

For what concerns the optical perturbation, we used totally absorbing objects, i.e. black cylinders made of Polyvinyl chloride (PVC) with different volumes. It was demonstrated in [39,40] that small totally absorbing objects are suitable to reproduce with any realistic absorption inhomogeneity with high reliability and reproducibility. More in detail, in a medium with a background characterized by a given  $\mu'_s$ , an Equivalence Class of absorbing perturbations characterized by different shapes and volumes can be defined. All perturbations under this Equivalence Class affect the DTOF in the same way for any choice of geometry (e.g.  $\rho$ ),  $\mu_a$  of the background and position of the inhomogeneity within the medium. For this reason, a totally absorbing object with a peculiar volume (Equivalent Black Volume – EBV –) can be used as a representative of an equivalent class of absorbing perturbations. It is worth to note that the use of the EBV is not perfectly valid for black objects with a very small volume ( $\leq 50 \text{ mm}^3$ ) and for shallower depths ( $\leq 10 \text{ mm}$ ). We adopted the EBV approach for its simplicity, reliability and high reproducibility of the measurements among different laboratories. Hence, we made use of black cylinders (height equal to diameter) with a volume of 25, 50, 100, 250 and 500  $\text{mm}^3$ , which are, for a medium with a  $\mu'_s = 10 \text{ cm}^{-1}$ , equivalent to realistic inclusions of volume 1000  $\text{mm}^3$  with a  $\Delta\mu_a$  of 0.0065, 0.0100, 0.0162, 0.0362 and 0.0952  $\text{mm}^{-1}$ , respectively [40].

### 2.2.2. Measurement strategy and data analysis

For each background medium, measurements were carried out at several  $\rho$  (namely 2, 4, 6, 8, 10, 15, 20, 25 and 30 mm) so as to compare results achieved with both the short distance approach (i.e.  $< 15 \text{ mm}$ ) and the classical ones. Once the  $\rho$  was set, the perturbation was aligned half way between the source and injection fibers and its depth ( $Z$ ) was taken as the distance between half of the cylinder height and the surface of the liquid. The inclusion was moved in depth ( $Z$  from 5 to 30 mm at step of 2.5 mm) through a motorized axis controlled

by the acquisition software. For each depth, 8 different portions (hardware gates) of the DTOF curves were acquired. This was done by changing the delay of the signal that triggers the generation of the 5 ns window hardware gate. For each delay, 5 repetitions of 1 s were recorded.

In the measurements, the effect of the optical perturbation was studied only on the phantom with  $\mu_a = 0.1 \text{ cm}^{-1}$  and  $\mu'_s = 10 \text{ cm}^{-1}$ .

For what concerns data analysis, the repetitions were summed up to increase the signal to noise ratio.

### 2.3. Simulations

The effect of a localized absorption perturbation was simulated using an 8th-order perturbative solution of the Radiative Transfer Equation under the diffusion approximation and the Extrapolated Boundary conditions [41]. The theoretical DTOF was convoluted with different IRFs to simulate the effect of the measurement apparatus. The finite count rate of the measurement system was taken into account by limiting the maximum number of counts per DTOF to  $10^6$  counts/s. Also, hardware time-gating used to suppress early photons and avoid saturation of the count rate at short  $\rho$  was simulated by slicing the DTOF before applying the count rate limitations. A realistic estimate of the DTOF amplitude (i.e. number of counts) was derived from the objective assessment of the system responsivity – as defined in the BIP Protocol [31] – converting the reflectance signal exiting the medium into detected counts. This information was then used to properly add shot noise to the simulated DTOFs.

The simulator consisted in an external framework with 4 iterators permitting to arbitrarily change different parameters in a range (e.g. background optical properties, absorption perturbation, features of the IRF, location of the inhomogeneity) and a central kernel performing the calculus of the homogeneous and perturbed DTOF. The external iteration framework was written in Matlab, while the kernel was compiled in C for computational efficiency. A typical simulation scenario, involving around 25000 points, is run automatically in about 10 minutes on a standard PC.

The standard value of the several parameters considered in the simulations are listed in Table 1 and, unless differently stated, they are valid for all simulations presented.

**Table 1. List of the parameters used in simulations and default values.**

Value	Units	Default value
Fast Tail Amplitude ( $A_1$ )	Decades below IRF peak	1
Fast Tail Slope ( $\tau_1$ )	ps	80
Memory tail amplitude ( $A_2$ )	Decades below the IRF peak	5
Memory tail slope ( $\tau_2$ )	ps	1800
Full-Width Half Maximum (FWHM)	ps	148.7
Acquisition time	s	1
Laser power	mW	100
Dark Count Rate (DCR)	counts per second	$100 \cdot 10^3$
Afterpulsing probability (AP)	%	2
Responsivity	$\text{mm}^2\text{sr}$	$3.014 \cdot 10^{-5}$
Background absorption coefficient ( $\mu_a$ )	$\text{mm}^{-1}$	0.01
Background scattering coefficient ( $\mu'_s$ )	$\text{mm}^{-1}$	1
Optical perturbation ( $\Delta \mu_a$ )	$\text{mm}^{-1}$	0.01

### 2.4. Figures of merit

To evaluate the performances obtained both in measurements and simulations, we made use of two standardized figures of merits (contrast – C – and contrast-to-noise ratio – CNR –), which were defined in the nEUROPt protocol [35] to assess the sensitivity (i.e. detection

capabilities of a small absorption change) of a TD instrument. This choice is justified by the fact, as stated above, that this study is focused on measurements of heterogeneous media. Indeed, contrast and CNR are figures of merit devised to assess the capability of a system in detecting perturbations inside diffusive media (e.g. to distinguish a region where there is a brain activation or a tumor within a surrounding tissue). More in detail, the contrast is an indicator of the effect of perturbations (in this case only in absorption) on photon counts. However, photon counting is dominated by Poisson statistics and other effects due to instabilities of the system. Hence, the contrast is not sufficient to evaluate the detectability of perturbations. This is the reason why also CNR has been devised, as it measures the reliability of the contrast by comparing the variation of the number of photon counts with the fluctuations of the counts.

For the calculation of contrast and CNR, we made use of the so-called “time windowing” of the curve, meaning that contrast and CNR were computed for portions of the DTOF curve (“software gate”). For both measurements and simulations, the width of the software gates used was set at 500 ps, while their position (i.e. the delay of the rising edge of the gate, reported as  $t_g$  in the following equation) is referred to the peak of the IRF. Due to the structure of the simulator code, in the simulation study the software gate was opened at the beginning of the hardware one. For comparison purposes, the same strategy was applied also to experimental data analysis.

The contrast is defined as the absolute difference between the unperturbed (i.e. homogeneous medium) and perturbed (i.e. optical perturbation inside the medium) states, normalized by the unperturbed state. It was computed for all depths of the inclusions following Eq. (1) [35]:

$$C(t_g) = \frac{N_0(t_g) - N(t_g)}{N_0(t_g)} \quad (1)$$

where,  $N_0$  is the overall number of counts in the software gate in the unperturbed case, while  $N$  is referred to the perturbed state. For the measurements, the acquisition of the homogeneous case was performed moving the perturbation 4 cm in depth, where its effect was completely negligible.

The CNR was computed following the definition given in [35] and reported in Eq. (2):

$$CNR(t_g) = \frac{N_0(t_g) - N(t_g)}{\sigma(N_0(t_g))} \quad (2)$$

where the difference at the numerator is calculated over the 5 repetitions while  $\sigma(N_0(t_g))$  is the standard deviation of the number of counts in the homogenous case computed over the repetitions. It has to be noted that in simulation the only noise source is the photonic one [42] thus  $\sigma(N_0(t_g)) = \sqrt{N_0(t_g)}$  while in measurements the standard deviation term can be affected also by other elements such as instabilities of the system (e.g. laser power fluctuations).

### 3. Results and discussion

The study consists of two parts. First, a comparative study between contrast calculated from experimental data and simulated data is presented. Secondly, a comprehensive simulation study addressed to different parameters is presented. In particular, we extend the simulation to study the effects of the parameters which can be classified under three categories, namely i) *system parameters*, which includes the IRF features (e.g. diffusion tail amplitude and time constant, FWHM, etc.), average laser power, system responsivity and noise sources (dark

counts and afterpulsing probability); ii) *geometrical and optical parameters* such as the amount of the perturbation and its depth, the background optical properties of the medium and iii) *measurement strategies* namely source-detector separation, acquisition time and hardware gate opening delay.

For the sake of brevity, we discuss here two cases: i) the fast-tail slope and ii) the memory tail amplitude. These parameters, as reported in [32,33], represent the main limitation to the achievable performance in terms of contrast and maximum penetration depth inside the tissue. More in detail, the fast tail is responsible for the temporal spreading of photons which dilute the contrast, while the memory effect sets a limit to the dynamic range of the measurement. Additionally, those two parameters are intrinsic of the detector (they depend on the fabrication process), therefore it is not possible to tune them in real systems in order to appreciate their effect on the measurement performance. All the other dependences can be found in [Dataset 1](#), [Dataset 2](#), [Dataset 3](#), [Dataset 4](#), [Dataset 5](#), [Dataset 6](#), [Dataset 7](#), [Dataset 8](#), [Dataset 9](#), and [Dataset 10](#) reported at [43–52] and the main conclusions drawn are reported in Table 2.

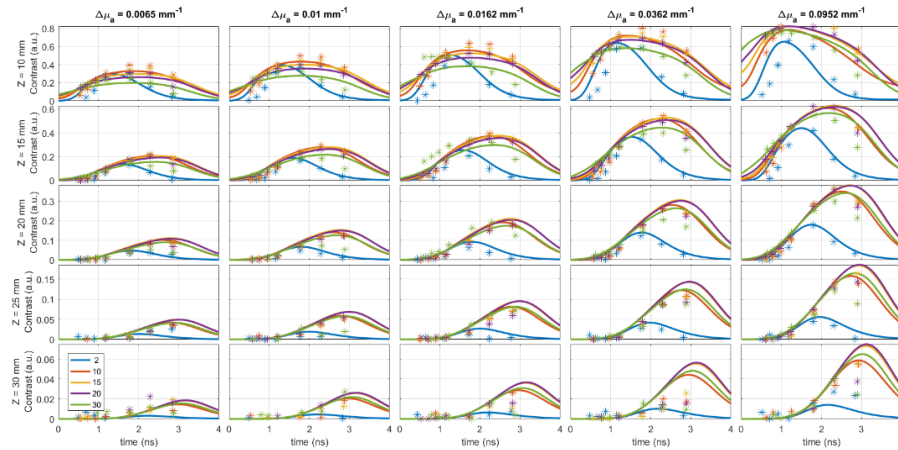


Fig. 2. Plot of contrast vs time (colors represent different source-detector distances), with change in depth of inclusion ( $Z$ ) along the rows and absorption perturbation ( $\Delta\mu_a$ ) along the columns. The experimental points are reported as stars, while the continuous curves correspond to simulated values.

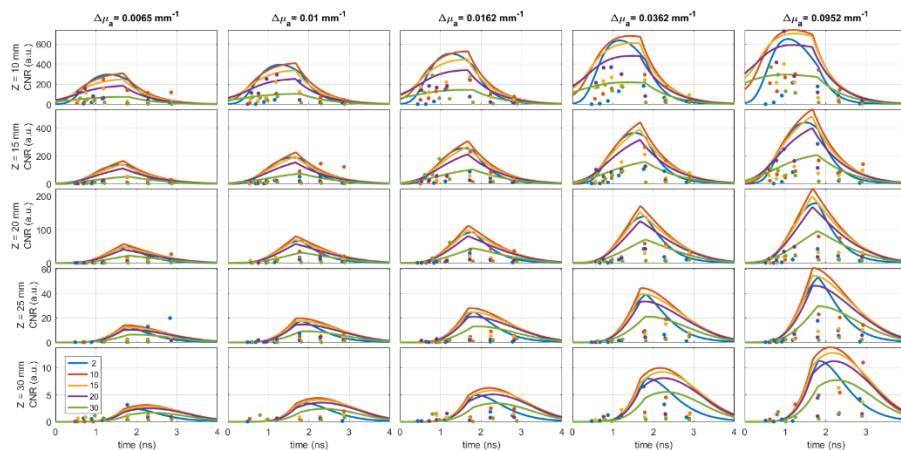


Fig. 3. Plot of CNR vs time (colors represent different source-detector distances), with change in depth of inclusion ( $Z$ ) along the rows and absorption perturbation ( $\Delta\mu_a$ ) along the columns. The experimental curves correspond to simulated values.

Figure 2 reports plots of contrast vs time, at different depths of inclusion (rows) and absorption perturbation (columns). For each situation, the contrast for 5 different source-detector separations is reported (colors in each plot). Figure 3 reports the CNR in the same conditions. In each picture, contrast or CNR obtained from measurements (dots) and simulations (continuous curves) are compared. As it can be observed, there is a fair agreement between measurements and simulations in the case of contrast. Some discrepancies (mainly evident for larger source-detector distances) are most probably due to loss in counts which is experienced at late times for larger  $\rho$  and  $Z$  values. In the case of CNR however, the agreement is much worse as simulations only take into account fluctuations due to Poisson noise and not all the sources of instability that can affect real systems (such as fluctuations in laser power, spurious leakage of room light, etc.). Hence, the quantification of CNR from simulations should be only considered as the maximum CNR one should expect by operating a system with perfect stability.

For what concerns the CNR, we can see a trend similar to the one of contrast, meaning that as the optical perturbation increases its value, we can observe a peaking of the CNR curve, as well as a (slight) increase in the amplitude. On the other hand, the peak of the CNR moves to later times when the inclusion is posed deeper. It is worth noting that CNR curves are not as smooth as contrast ones. This behavior is due to the implementation of the time-gated technique, which allows to adjust the optical power injected into the medium under investigation in each hardware gate, depending on its delay with respect to  $t = 0$  ns. When the hardware gate is opened at early delays, the signal in the DTOF is so high that it must be attenuated not to exceed the maximum count rate allowed by the system (“count rate limitation” in Sect. 2.3). On the contrary, at later delays, the signal in the DTOF is orders of magnitude lower (in particular at short  $\rho$ ), thus reaching a condition where the attenuation of the signal is no more needed to fit the maximum count rate. Hence, the sharp corner in the CNR curves is due to the transition between two different regimes of operation, on the left (early times) the signal is adjusted at each delay of the hardware gate not to exceed the maximum count rate, while on the right (late times) the signal is kept constant. This effect is not present in contrast curves just because they do not depend on the number of counts.

It can also be noticed that the change in contrast upon increasing  $\Delta\mu_a$  (moving along columns) is dependent not only on  $Z$  (rows) but also on  $\rho$ . By moving along columns, we can see that contrast increases with increasing  $\Delta\mu_a$ , as expected. Indeed, the probability of a photon having encountered the inclusion increases with increasing absorption perturbation.

For this reason, keeping the other conditions equal (i.e. depth and source-detector distance), the contrast curves are supposed to be rescaled by a factor given by the different  $\Delta\mu_a$ . If moving along the rows (i.e. perturbation buried more in depth), the contrast decreases due to the spreading of the sensitivity profile of photons. Additionally, the peak corresponding to maximum contrast shifts towards longer time. This is due to the fact that re-emission time of photons encodes the mean probed depth. Thus, as it is well known working in the TD, for superficial inclusions the maximum contrast is provided by photons re-emitted earlier in time compared to those for the deeper inclusions. The contrast decrease for largest arrival times is mainly due to the memory tail (in particular for shorter  $\rho$ ) and to the background noise floor given by both DCR and AP (in particular for larger  $\rho$ ).

Crucially, under the effect of the memory tail, we observe that the maximum contrast is not obtained for small  $\rho$  values, as it was theorized in [24] for ideal systems, but for intermediate values (i.e.,  $\rho = 10$ -15 mm). This can be ascribed to the fact that memory tail limits the dynamic range of the system and hence clamps down the contrast at late times. However, since memory is a signal-dependent phenomenon [34], the reduction in contrast is maximum for small  $\rho$  values, where the early arriving photons signal is maximum [24].

As stated above, the decrease in contrast for larger  $\rho$  is due to the detector background noise. Indeed, it is not possible to increase the power injected endlessly. Thus, the ratio between the curve and the noise floor decreases at later delays, demoting the contrast in

particular at large  $\rho$ . Such an effect of the noise floor can be better appreciated in the figures reporting the simulations varying the noise floor (see [49,50].) and also in those reporting the variations in contrast upon a variation of the injected power (see [47].).

Tables 3-7 in the Appendix report the relative errors between measurements and simulations for each point of Fig. 2 and Fig. 3. In general, apart from the discrepancies discussed above, it is possible to verify a fair concordance, having in many cases errors in the order of 10-20%.

Measured and simulated data have been also compared by changing 5 different optical properties of the background medium, keeping constant this time the black cylinder perturbation (i.e. the one with a  $100 \text{ mm}^3$  volume, which features, for a medium with  $\mu'_s = 10 \text{ cm}^{-1}$ , a  $\Delta\mu_a = 0.0162 \text{ mm}^{-1}$  in a volume  $1000 \text{ mm}^3$ ). Errors are consistent with the previously discussed study performed with different perturbations. Results, not reported here for brevity, are available at [52].

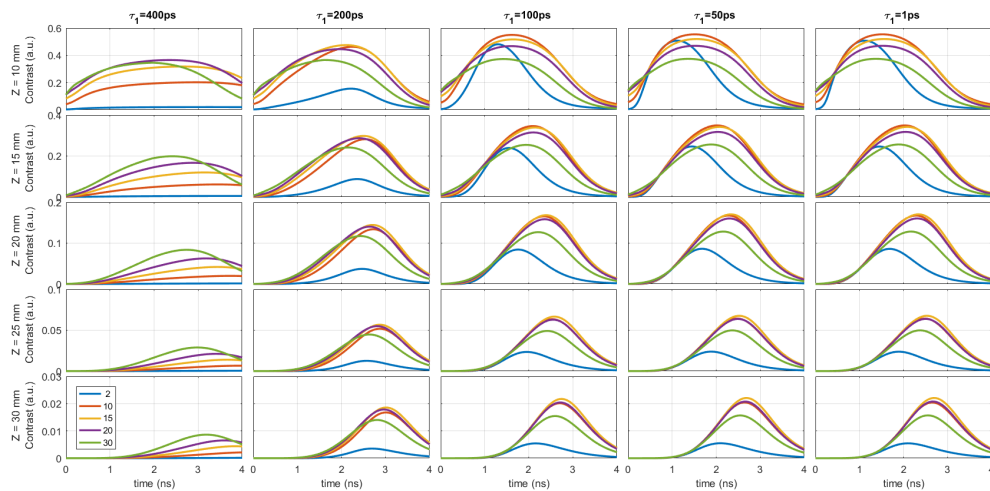


Fig. 4. Plot of Contrast vs time, with change in depth of inclusion ( $Z$ ) along the rows and diffusion tail slope ( $\tau_1$ ) along the columns.

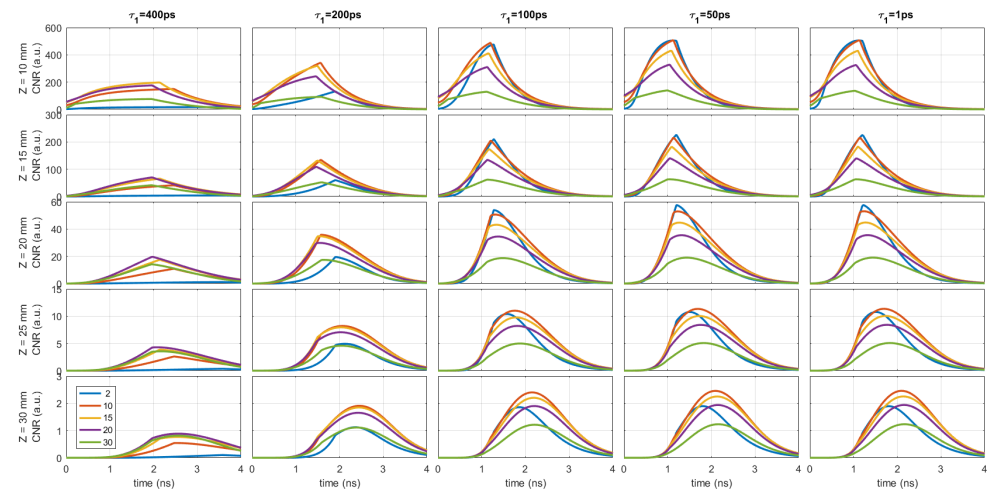


Fig. 5. Plot of CNR vs time, with change in depth of inclusion ( $Z$ ) along the rows and diffusion tail slope ( $\tau_1$ ) along the columns.

Figure 4 (Fig. 5) shows the simulated contrast (CNR) vs time for different source-detector separations upon a variation of the depth (rows) of the inclusion (with  $\Delta\mu_a = 0.0162 \text{ mm}^{-1}$ ) and diffusion tail slope ( $\tau_1$ ) of the IRF (columns). As the diffusion tail slope decreases (i.e. the IRF get sharper with a fast decrease of the first diffusion tail), we observe a narrowing of the contrast curves due to the reduced contamination of the early photons in a temporal region of the curve where only contribution of late photons are expected, as predicted in [32]. Indeed, for shorter  $\rho$ , the reflectance curve is less broadened and so, in the convolution process, a large diffusion tail can dominate when compared to the ideal (i.e. IRF equal to a delta Dirac) response of the medium. A reasonable upper threshold for  $\tau_1$  is around 200 ps where there are no significant effects at least for  $\rho \geq 10 \text{ mm}$ . Even in the almost ideal case of  $\tau_1 = 1 \text{ ps}$  (last column) the contrast at the shorter  $\rho$  is suboptimal because of the memory effect. We recall here that simulations are performed varying specific parameters at a time (here  $\rho$ ,  $Z$  and  $\tau_1$ ) while keeping the others (e.g. *memory effect*) fixed at a given pivotal position, reported in Table 1.

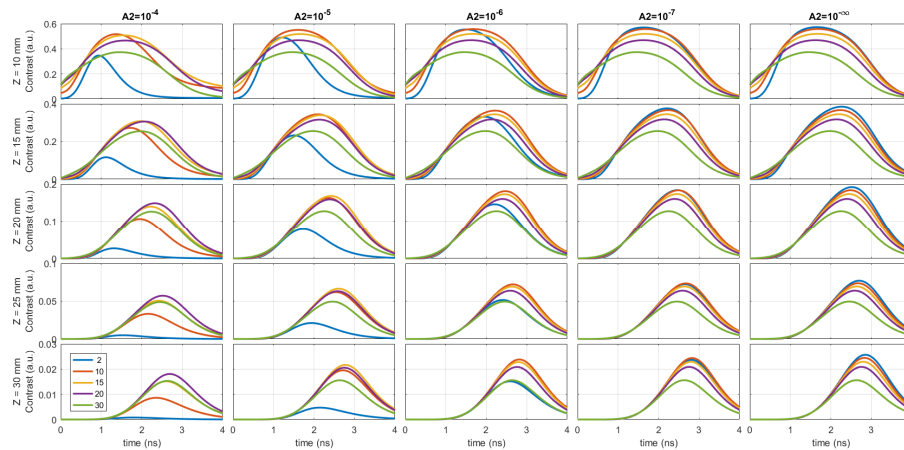


Fig. 6. Plot of Contrast vs time, with change in depth of inclusion ( $Z$ ) along the rows and memory amplitude ( $A_2$ ) along the columns.

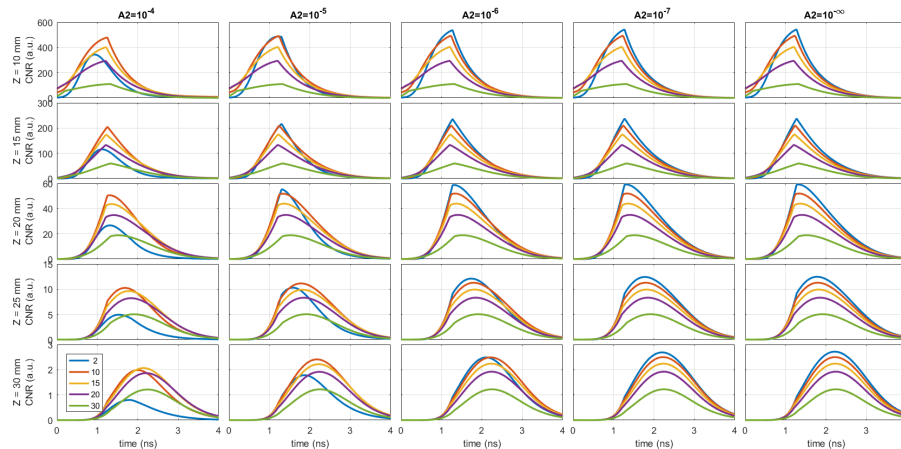


Fig. 7. Plot of CNR vs time, with change in depth of inclusion ( $Z$ ) along the rows and memory amplitude ( $A_2$ ) along the columns.

The effect of diffusion tail slope with different background optical properties ( $\mu_a, \mu_s'$ ) and  $\Delta\mu_a$  can be found at [45]. The threshold condition for  $\tau_1$  is changing (and getting stricter)

for more harsh environments (higher  $\mu_a$ , lower  $\mu_s'$ ). Partially, this can be compensated by increasing  $\rho$ .

In Fig. 6 (Fig. 7) we see the variation of contrast (CNR) with  $Z$  (rows) and memory tail amplitude ( $A_2$ , columns), keeping the memory tail slope fixed at 1800 ps, which is the experimental value recovered using the fast-gated SPAD detector in the system in Fig. 1(a). Here  $A_2 = 10^{-4}, 10^{-5}, 10^{-6}, 10^{-7}$  corresponds to IRF curves where the memory tail is attached 4, 5, 6 and 7 orders of magnitude below the peak, respectively and  $10^{-\infty}$  corresponds to IRF without any memory tail.

As it is evident from the figure, the contrast improves by lowering the memory tail. The improvement is largest for small  $\rho$ , as the contribution of memory effect to the background noise increases with increase in the number of early photons impinging on the detector. Hence, generally speaking, we do not obtain a higher contrast at null source-detector separation by using detectors which have a memory tail amplitude even 7 decades below the peak. Anyway, it has to be noted that the larger the memory tail amplitude the more detrimental the effect on the contrast. This fact shows therefore that the memory effect sets the main limitation to the measurement performance in time gated systems. Here, a reasonable threshold is observed with a memory effect at least 6 decades below the peak. Unfortunately, this parameter can hardly be controlled even at the level of device fabrication. The same conclusions can be drawn looking at the CNR trend upon a variation of the memory tail amplitude, which are shown in Fig. 7.

The effect of memory tail amplitude with different background optical properties ( $\mu_a$ ,  $\mu_s'$ ) and  $\Delta\mu_a$  can be found at [46]. The trend of contrast and CNR upon a variation of  $Z$ , ( $\mu_a$ ,  $\mu_s'$ ) and  $\Delta\mu_a$  for several values of FWHM of the IRF, optical responsivity [31], incident laser power, dark count rate, afterpulsing, acquisition time and system responsivity can be found in All the other dependences can be found in [Dataset 1](#), [Dataset 2](#), [Dataset 3](#), [Dataset 4](#), [Dataset 5](#), [Dataset 6](#), [Dataset 7](#), [Dataset 8](#), [Dataset 9](#), and [Dataset 10](#) reported at reported at [43–52]. For the sake of the synthesis, the key findings including also these additional parameters are summarized in Table 2.

#### 4. Conclusions

The null or small source-detector separation approach ( $\rho \sim 0$ ) has been proposed in time-domain diffuse optics more than ten years ago as a promising way to maximize measurement performances in terms of overall amount of detected signal, contrast produced by localized absorption perturbations inside the scattering medium and spatial resolution related to the perturbation localization. This could be achieved under the hypothesis to make use of a measurement system characterized by an ideal temporal response, free from slow tails or any source of background noise [24]. However, implementations in real systems always showed limited advantages [25]. In this work, using the state of the art system for the implementation of the small source-detector separation approach, we experimentally studied the effect of the source-detector distance choice and perturbation size and depth. The response function of our system, far different from a Dirac delta, as expected, gave rise to a compression of the contrast produced by the perturbation when the system is used at the smallest  $\rho$  (2 mm). Since also the contrast at the largest  $\rho$  (30 mm) is limited due to the broadening of the sensitivity shape, it turns out that in most cases the choice of a  $\rho$  of 10 or 15 mm represents the best condition to maximize both contrast and contrast-to-noise ratio.

**Table 2. Parameters analyzed in the simulation study and their impact on the contrast and CNR.**

	Parameter (increasing)	Impact		Effect	See
		short $\rho$	large $\rho$		
SYSTEM	Full Width at Half Maximum (FWHM)	High	Low	Contrast: IRF peak shifts towards late times for short $\rho$ . Depends strongly on background parameters. CNR: decreases	[43]
	Fast tail amplitude ( $A_1$ )	Low	Low	Contrast: very slight increase. CNR: very slight increase.	[44]
	Fast tail slope ( $\tau_1$ )	High	High	Contrast: curves broaden and their amplitude reduce. Strong effect at short $\rho$ . CNR: curves decrease and broaden.	[45]
	Memory tail amplitude ( $A_2$ )	High	Low	Contrast: strong reduction for small $\rho$ , almost no effect for large ones. CNR: reduction for small $\rho$ , no effect for large ones.	[46]
	Average laser power	High	High	Contrast: increases. For large $\rho$ , it tends to flatten at late times. CNR: increases.	[47]
	Optical responsivity	High	High	Contrast: increases at late times in particular for large $\rho$ , where it tends to flatten. CNR: increases.	[48]
	Dark count rate (DCR)	Low	High	Contrast: reduces at late times, in particular at large $\rho$ . CNR: almost no effect.	[49]
	Afterpulsing probability (AP)	Low	Low	Contrast: no effect. CNR: no effect.	[50]
GEOM	Perturbation depth	High	High	Contrast: decreases and its peak shifts towards late times. CNR: decreases and its peak shifts towards late times.	[43–51]
OPTICAL	Background absorption	High	High	Contrast: decreases (in particular at late times) and curves become narrower. CNR: decreases (in particular at late times) and curves become narrower.	[43–51]
	Background scattering	High	High	Contrast: decreases and its peak shifts towards later times. CNR: decreases and its peak shifts towards later times.	[43–51]
	Amount of absorption perturbation	High	High	Contrast: increase almost independently of the $\rho$ . CNR: increases almost independently of the $\rho$ .	[43–51]
STRATEGY	Source-detector separation	High	High	Contrast: generally, in presence of slow tails (e.g. memory effect), intermediate $\rho$ (1-1.5 cm) gives higher contrast. CNR: generally, in presence of slow tails (e.g. memory effect), intermediate $\rho$ (1-1.5 cm) gives higher CNR.	Colors in all graphs
	Gate opening delay	High	High	Contrast: Strong and different effects depending on many other parameters. CNR: Strong and different effects depending on many other parameters.	x axis of all graphs
	Acquisition time	High	High	Contrast: no change. CNR: increases as the square root of acquisition time.	[51]

The same scenarios were also studied in-silico, confirming the previous findings about optimal values for the source-detector distance. Hence, simulations allowed us to extend the study and understand the effects of different non-idealities in the instrument response function, simulating changes in different regions of the system temporal response (e.g. full-width at half maximum, diffusion tail amplitude and slope and memory effect amplitude). Similarly, other systems features were studied (e.g. dark count rate), as well as effects of the measurement geometries, optical properties and measurements strategies.

Among the main findings, it is evident that the memory effect represents the main limiting factor for the use of a small source-detector separation approach. Indeed, when the memory effect is particularly high ( $A_2 > 10^{-7}$ ), it is capable to force the choice of an intermediate  $\rho$  (e.g. 10-15 mm) to obtain the best contrast, thus completely reverting the direction of previous findings of [24], whose validity is not questioned here, since the study was intentionally restricted to ideal systems. A summary of the key findings of this work, and the relevance of different parameters is reported in Table 2.

Thanks to the broad spectrum of cases reported here, this work can represent a reference for scientists interested in the use of time-domain diffuse optics systems, allowing them to select the best measurement strategy and probe geometry depending on their specific problem under study and on the specific features of their hardware. Even more interestingly, this paper provides figures of merit for the evaluation of the performance of novel technologies under development (lasers, detectors, timing circuits) in the field of time-domain diffuse optics, permitting the estimation of the effects of hardware features on measurements results.

## Appendix

In this section, the errors between measured and simulated data of Figure 2 (for contrast) and Figure 3 (for CNR) are reported. They have been computed as:

$$error (\%) = 100 * \frac{\tilde{x} - x}{\tilde{x}} \quad (3)$$

where  $\tilde{x}$  is the measured value (of either contrast or CNR) and  $x$  is the simulated one. Table 3–7 report all the errors, depending on the depth of the perturbation. The value is not reported, being not meaningful, in conditions where the measured CNR is lower than 1 or where the number of counts inside the software gate is lower than 1000 for measured data.

**Table 3. Percentage error between measurements and simulations computed for both contrast and CNR for the depth of the inclusion of 10 mm.**

$\rho$	Gate 1 C/CNR	Gate 2 C/CNR	Gate 3 C/CNR	Gate 4 C/CNR	Gate 5 C/CNR	Gate 6 C/CNR	Gate 7 C/CNR	
$\Delta\mu_a = 0.0952$ $\text{mm}^{-1}$	2	-370/<-500	-182/<-500	-62/<-500	2/-200	36/-113	38/-3	49/-106
	10	-19/-185	-4/-413	5/-172	12/-144	22/-50	32/-24	31/-43
	15	-6/21	-3/-202	1/-72	5/-219	11/<-500	15/-222	-2/-120
	20	-2/67	-3/-34	-1/20	1/-113	5/-280	4/<-500	-28/-97
	30	-4/22	-5/1	-5/-128	-3/-150	-3/<-500	-13/-412	-67/-379
$\Delta\mu_a = 0.0362$ $\text{mm}^{-1}$	2	-425/<-500	-236/<-500	-84/<-500	-12/-388	20/-151	19/-108	19/-5
	10	-51/<-500	-28/-429	-10/-306	2/-267	13/-81	19/-22	20/-66
	15	-21/-157	-16/-123	-6/-113	1/-212	7/-97	8/-308	-2/23
	20	-5/-70	-7/-15	-2/-22	1/-60	3/-371	2/-467	-21/-166
	30	4/-11	3/-6	2/-56	2/-26	3/<-500	-6/<-500	-42/-134
$\Delta\mu_a = 0.0162$ $\text{mm}^{-1}$	2	<-500/<-500	-259/<-500	-133/<-500	-28/-227	2/-65	-17/-56	5/-46
	10	-63/-437	-36/-460	-11/-230	3/-197	13/-102	17/-71	16/11
	15	-10/-38	-12/-159	-3/-119	5/-86	11/-48	12/-141	6/-54
	20	0/-49	-3/-38	2/-70	6/-72	9/-300	10/-477	3/-242
	30	40/4	34/58	28/-110	22/-147	8/<-500	-12/<-500	-59/-299
$\Delta\mu_a = 0.0100$ $\text{mm}^{-1}$	2	<-500/<-500	-395/<-500	-121/<-500	-26/<-500	14/-38	9/-207	-11/-81
	10	-92/<-500	-51/<-500	-18/-453	1/-246	13/-196	15/-92	14/-13
	15	-33/-256	-25/<-500	-7/-290	4/-43	11/-129	10/-284	0/-86
	20	-3/-33	-3/-67	3/16	9/21	11/-379	9/-380	-6/-137
	30	20/-8	17/-30	16/-144	18/-24	12/<-500	-10/<-500	-73/-362
$\Delta\mu_a = 0.0065$ $\text{mm}^{-1}$	2	-/-	-333/<-500	-105/<-500	-13/-405	20/-77	16/-79	23/-21
	10	-114/<-500	-61/<-500	-19/<-500	4/-11	17/-82	19/3	14/65
	15	-36/-291	-25/-46	-7/-484	7/-44	15/<-500	17/-392	2/-75
	20	1/15	3/18	9/-78	13/-156	17/<-500	13/<-500	-43/-259
	30	23/16	21/-10	20/-70	18/-317	19/<-500	7/<-500	-92/-203

**Table 4. Percentage error between measurements and simulations computed for both contrast and CNR for the depth of the inclusion of 15 mm.**

$\rho$	Gate 1 C/CNR	Gate 2 C/CNR	Gate 3 C/CNR	Gate 4 C/CNR	Gate 5 C/CNR	Gate 6 C/CNR	Gate 7 C/CNR	
$\Delta\mu_a = 0.0952$ $\text{mm}^{-1}$	2	-/-	<-500/<-500	-156/<-500	-29/-367	6/-37	-18/-73	-69/-335
	10	-103/<-500	-65/-237	-24/<-500	-1/-370	10/-156	11/-121	-3/50
	15	-39/-125	-27/-463	-13/-416	1/-201	8/-443	4/-218	-26/25
	20	-2/-29	-8/-11	-4/0	3/-95	7/-199	-1/<-500	-40/-195
	30	9/16	3/-21	-1/-131	1/-175	1/<-500	-12/-266	-69/-219
$\Delta\mu_a = 0.0362$ $\text{mm}^{-1}$	2	-219/<-500	<-500/<-500	-167/<-500	-48/-413	0/-223	-15/-42	-36/-307
	10	-192/<-500	-123/<-500	-65/<-500	-24/-295	0/-42	5/-5	0/-17
	15	-87/-439	-76/-191	-44/-232	-19/-85	-3/-56	0/-288	-17/18
	20	-35/20	-43/-146	-29/-114	-16/-132	-2/-115	-3/-437	-33/-261
	30	-11/21	-10/-96	-15/-53	-10/-33	-6/<-500	-11/<-500	-51/-197
$\Delta\mu_a = 0.0162$ $\text{mm}^{-1}$	2	-/-	-/-	-433/<-500	-81/<-500	-21/-190	-58/-154	-84/-193
	10	-87/<-500	-110/-434	-80/<-500	-30/-245	0/-25	6/-69	4/-53
	15	-60/-213	-83/-150	-57/-383	-27/-219	0/-343	3/-103	-2/-125
	20	-55/-135	-68/-188	-44/-79	-24/-159	-1/<-500	1/<-500	-6/-274
	30	50/51	43/33	38/68	34/-137	22/<-500	6/-379	-50/-72
$\Delta\mu_a = 0.0100$ $\text{mm}^{-1}$	2	-/-	-440/<-500	-284/<-500	-93/-459	-11/-251	-5/-26	-31/-137
	10	-264/<-500	-258/<-500	-126/<-500	-51/<-500	-4/-122	3/33	3/69
	15	-127/-365	-148/<-500	-66/<-500	-33/-315	0/<-500	4/-239	-11/-174
	20	-61/-133	-66/<-500	-43/-263	-25/-403	0/<-500	3/-358	-21/-321
	30	-35/-39	-22/-104	-17/-129	0/-407	-2/<-500	-19/<-500	-103/-423
$\Delta\mu_a = 0.0065$ $\text{mm}^{-1}$	2	5/<-500	<-500/<-500	-396/<-500	-65/-469	-2/-162	-18/-198	-112/-57
	10	-255/<-500	-204/-487	-118/-372	-47/-383	-4/-199	6/-190	5/4
	15	-164/-327	-128/<-500	-114/<-500	-33/-251	-2/-143	6/-257	-6/-160
	20	<-500/<-500	-396/-239	-97/-277	-7/-179	11/<-500	8/<-500	-37/-381
	30	-24/-12	-30/-169	-15/-71	-2/-447	13/<-500	-31/<-500	-74/-275

**Table 5. Percentage error between measurements and simulations computed for both contrast and CNR for the depth of the inclusion of 20 mm.**

	$\rho$	Gate 1	Gate 2	Gate 3	Gate 4	Gate 5	Gate 6	Gate 7
		C/CNR	C/CNR	C/CNR	C/CNR	C/CNR	C/CNR	C/CNR
$\Delta\mu_a = 0.0952$ $\text{mm}^{-1}$	2	-111/<500	<500/<500	-142/<500	-65/<500	-2/318	-28/-241	-28/-206
	10	-416/<500	-157/<500	-89/<500	-30/-434	6/-150	10/-48	-6/-77
	15	-206/-391	-114/<500	-58/-246	-23/2	5/-453	3/-244	-25/-55
	20	-23/-12	-38/-242	-26/-59	-10/-90	4/<500	1/<500	-37/-139
	30	-4/10	-13/-20	-9/-69	0/-140	-3/<500	-11/-498	-51/-364
$\Delta\mu_a = 0.0362$ $\text{mm}^{-1}$	2	-/-	-71/<500	<500/<500	-108/<500	-15/-231	-24/-271	-46/-96
	10	-/-	-/-	-206/<500	-74/<500	-16/-163	-3/-64	-9/-40
	15	-155/-224	-147/-395	-136/-440	-51/-310	-19/-371	-8/-77	-25/-29
	20	-13/-52	-137/-74	-100/-353	-50/-347	-10/-168	-5/<500	-34/-194
	30	8/-106	-14/-115	-45/-129	-14/-477	-28/<500	-21/<500	-52/-140
$\Delta\mu_a = 0.0162$ $\text{mm}^{-1}$	2	89/-139	70/-362	-159/<500	-136/<500	-51/-215	-89/-289	-292/<500
	10	-/-	-/-	-60/-496	-96/<500	-23/-164	-7/-59	-5/13
	15	<500/<500	-95/-381	-111/-322	-71/-227	-26/-362	-17/-296	-5/-159
	20	-309/<500	-94/-161	-141/-345	-73/-350	-47/<500	-17/<500	-12/-193
	30	36/-43	39/48	25/-51	27/66	28/<500	15/<500	-35/-286
$\Delta\mu_a = 0.0100$ $\text{mm}^{-1}$	2	-/-	-/-	-/-	-289/<500	-40/-288	-52/-70	-60/-142
	10	-/-	-5/-149	-250/<500	-83/<500	-40/-115	-12/-51	-8/-3
	15	18/60	-94/<500	-379/<500	-91/-95	-28/-404	-18/<500	-21/-105
	20	-426/<500	-335/<500	-90/-422	-74/-264	-30/-440	-22/-210	-20/-472
	30	-174/-192	-/-	-163/-448	-53/-55	-17/<500	-56/<500	-129/-349
$\Delta\mu_a = 0.0065$ $\text{mm}^{-1}$	2	86/-267	13/<500	-/-	<500/<500	-42/-389	7/-98	51/15
	10	-/-	-/-	-74/<500	-185/<500	-38/-255	-10/-193	-9/40
	15	-143/-349	-117/-464	-227/<500	-373/<500	-33/-361	-24/-315	-33/-257
	20	-81/-33	-114/-329	-405/-431	-161/<500	-53/<500	-10/<500	-63/-369
	30	-137/-389	-282/<500	-85/-458	-73/<500	-58/<500	-46/<500	-146/-273

**Table 6. Percentage error between measurements and simulations computed for both contrast and CNR for the depth of the inclusion of 25 mm.**

	$\rho$	Gate 1	Gate 2	Gate 3	Gate 4	Gate 5	Gate 6	Gate 7
		C/CNR						
$\Delta\mu_a = 0.0952$ $\text{mm}^{-1}$	2	77/-384	88/20	-28/<500	-115/<500	-20/-199	-37/-201	<500/<500
	10	10/-174	-/-	-/-	-103/<500	-12/-159	3/-115	-10/-62
	15	-/-	-/-	-/-	-208/<500	-25/<500	-7/-272	-13/-133
	20	<500/-181	-372/<500	-46/-161	-24/-151	-9/<500	-11/<500	-29/-269
	30	35/29	-335/-395	2/-111	10/-2	-36/<500	-12/<500	-84/<500
$\Delta\mu_a = 0.0362$ $\text{mm}^{-1}$	2	99/84	59/-204	-77/<500	-99/<500	-41/-350	-52/-290	-273/<500
	10	63/-108	-/-	-273/<500	-91/<500	-34/-372	-18/-82	-11/-176
	15	-/-	-/-	-/-	-181/<500	-53/-474	-21/-114	-36/-147
	20	-337/<500	-/-	-/-	-231/<500	-27/<500	-19/<500	-52/-251
	30	49/47	-/-	2/-83	-45/-146	-76/<500	-16/<500	-42/-170
$\Delta\mu_a = 0.0162$ $\text{mm}^{-1}$	2	-/-	97/72	-/-	-289/<500	-98/<500	<500/<500	-213/<500
	10	96/82	53/-92	-90/<500	-24/-460	-79/-497	-24/-155	-14/-141
	15	44/0	-/-	-/-	-63/-329	-78/<500	-25/-283	-30/-201
	20	91/89	-68/-130	55/34	-68/-322	-57/<500	-63/<500	-55/-481
	30	-/-	-128/-50	-19/-259	-5/-69	8/<500	1/<500	-11/-125
$\Delta\mu_a = 0.0100$ $\text{mm}^{-1}$	2	99/85	84/-138	-123/<500	-313/<500	-119/-143	-113/-373	-/-
	10	-/-	94/74	-/-	-/-	-92/-341	-29/-221	-16/-22
	15	-/-	-/-	-/-	-31/-222	-116/<500	-39/<500	-25/-165
	20	76/57	59/75	-179/-229	12/-77	-83/<500	-15/-201	-21/-324
	30	-194/-266	-/-	-/-	-375/<500	12/<500	-297/<500	-205/<500
$\Delta\mu_a = 0.0065$ $\text{mm}^{-1}$	2	100/94	95/34	62/-118	-7/-344	-268/<500	39/40	76/86
	10	-/-	74/-73	-/-	-4/-258	-127/-488	-58/-434	-13/-152
	15	-/-	-/-	-/-	-/-	-49/<500	-97/<500	-45/-85
	20	-/-	-/-	-/-	-/-	<500/<500	-57/<500	-36/-267
	30	-/-	-/-	-/-	39/-184	-282/<500	-7/<500	-/-

**Table 7. Percentage error between measurements and simulations computed for both contrast and CNR for the depth of the inclusion of 30 mm.**

	$\rho$	Gate 1 C/CNR	Gate 2 C/CNR	Gate 3 C/CNR	Gate 4 C/CNR	Gate 5 C/CNR	Gate 6 C/CNR	Gate 7 C/CNR
$\Delta\mu_s = 0.0952$ $\text{mm}^{-1}$	2	100/98	88/-19	92/16	-286/<-500	29/-150	49/60	65/11
	10	98/92	97/87	-/-	62/21	6/-161	-25/-143	-6/19
	15	-/-	-/-	-/-	-/-	-86/<-500	-10/-99	-28/-155
	20	-/-	-/-	-/-	-/-	-73/<-500	-5/<-500	-90/-479
	30	-/-	89/91	-100/-395	2/-51	-30/<-500	-3/-377	-162/-467
$\Delta\mu_s = 0.0362$ $\text{mm}^{-1}$	2	100/99	99/91	98/87	71/-13	-6/-11	-2/-104	-99/-271
	10	-/-	-/-	-/-	62/-11	-100/-413	-42/-116	-162/-339
	15	98/96	82/66	-211/<-500	63/42	-365/<-500	-198/<-500	-105/-438
	20	-/-	94/91	-/-	16/0	-/-	-110/-464	-243/<-500
	30	-/-	86/77	52/-5	-/-	24/<-500	-106/<-500	-400/<-500
$\Delta\mu_s = 0.0162$ $\text{mm}^{-1}$	2	100/100	-/-	-/-	77/4	-/-	-48/-131	45/-87
	10	-/-	-/-	98/92	-/-	-106/-480	-40/-143	-9/-95
	15	-/-	-/-	96/90	77/19	-143/<-500	-45/<-500	-214/-237
	20	98/96	83/77	77/68	77/66	-243/<-500	-12/<-500	-105/-435
	30	-/-	97/97	87/68	37/38	<-500/<-500	-10/-465	<-500/<-500
$\Delta\mu_s = 0.0100$ $\text{mm}^{-1}$	2	100/99	-/-	-/-	-/-	-/-	-/-	-269/<-500
	10	100/100	-/-	-/-	-/-	-126/<-500	<-500/<-500	-10/-64
	15	-/-	-/-	92/52	-/-	-105/-295	-24/-349	-84/-163
	20	-/-	-/-	-/-	80/28	-/-	9/-462	-/-
	30	-/-	98/98	92/80	-/-	30/<-500	-63/<-500	22/-172
$\Delta\mu_s = 0.0065$ $\text{mm}^{-1}$	2	100/99	100/99	98/91	79/-3	76/28	-/-	-/-
	10	90/78	98/87	56/-40	87/52	9/-137	1/-165	-75/-98
	15	100/100	99/98	-/-	-/-	52/-80	16/-194	13/-99
	20	-/-	-/-	-/-	-/-	66/-404	60/-258	-2/-142
	30	-/-	-/-	97/95	93/63	45/-301	24/-352	-174/-212

## Funding

EC's H2020 Framework Programme (BITMAP 675332); European Union's Horizon 2020 research and innovation programme (731877, SOLUS: Smart Optical and UltraSound diagnostics of breast cancer, 654148 (Laserlab-Europe)).

## Acknowledgments

The authors wish to thank Davide Bianchi and Giulia Maffei for their help during experimental measurements. We acknowledge nEUROpt European Project and, in particular, Fianium Ltd for developing and making available the four-wave mixing laser source.

## Disclosures

The authors declare that there are no conflicts of interest related to this article.